Sensor array design of optically pumped magnetometers for accurately estimating source currents

Yusuke Takeda [a,b,*], Tomohiro Gomi [c], Ryu Umebayashi [c], Sadamu Tomita [c], Keita Suzuki [b], Nobuo Hiroe [b], Jiro Saikawa [c], Tatsuya Munaka [c], Okito Yamashita [a,b]

[a] Computational Brain Dynamics Team, RIKEN Center for Advanced Intelligence Project, 2-2-2 Hikaridai, Seika-cho, Soraku-gun, Kyoto, 619-0288, Japan
[b] Department of Computational Brain Imaging, ATR Neural Information Analysis Laboratories, 2-2-2 Hikaridai, Seika-cho, Soraku-gun, Kyoto, 619-0288, Japan
[c] Technology Research Laboratory, Shimadzu Corporation, 3-9-4 Hikaridai, Seika-cho, Soraku-gun, Kyoto 619-0237, Japan

ARTICLE INFO

ABSTRACT

An optically pumped magnetometer (OPM) is a new generation of magnetoencephalography (MEG) devices that is small, light, and works at room temperature. Due to these characteristics, OPMs enable flexible and wearable MEG systems. On the other hand, if we have a limited number of OPM sensors, we need to carefully design their sensor arrays depending on our purposes and regions of interests (ROIs). In this study, we propose a method that designs OPM sensor arrays for accurately estimating the cortical currents at the ROIs. Based on the resolution matrix of minimum norm estimate (MNE), our method sequentially determines the position of each sensor to optimize its inverse filter pointing to the ROIs and suppressing the signal leakage from the other areas. We call this method the Sensor array Optimization based on Resolution Matrix (SORM). We conducted simple and realistic simulation tests to evaluate its characteristics and efficacy for real OPM-MEG data. SORM designed the sensor arrays so that their leadfield matrices had high effective ranks as well as high sensitivities to ROIs. Although SORM is based on MNE, the sensor arrays designed by SORM were effective not only when we estimated the cortical currents by MNE but also when we did so by other methods. With real OPM-MEG data we confirmed its validity for real data. These analyses suggest that SORM is especially useful when we want to accurately estimate ROIs' activities with a limited number of OPM sensors, such as brain-machine interfaces and diagnosing brain diseases.

1. Introduction

Our brain activities produce very weak magnetic fields outside of our heads. By measuring these magnetic fields, we can examine brain activities with excellent temporal resolution on the millisecond order. Conventionally, the magnetic fields produced by our brains have been measured by magnetoencephalography (MEG) systems equipped with Superconducting QUantum Interference Devices (SQUIDs), such as the Elekta Neuromag Vectorview 306 system (Helsinki). These systems are large, placing more than 200 sensors over the whole head, and liquid helium is housed around the sensors to cool them.

Recently, a new device was introduced (Shah and Wakai, 2013), an optically pumped magnetometer (OPM), which has attracted great interest from the MEG community (Boto et al., 2016; 2017; Brookes et al., 2022; Ilmoniemi and Sarvas, 2019; Tierney et al., 2019). An OPM sensor is small, light, and works at room temperature without cryogenic cooling. Due to these characteristics, OPMs enable flexible and wearable MEG systems, which allow us to measure MEGs under such severe situations that include the brain activities of children and during movements (Seymour et al., 2021). Furthermore, we can put OPM sensors on the head, yielding high sensitivity to brain activities (Boto et al., 2017; Iivanainen et al., 2017).

On the other hand, because this technology is still in its early stage, well-established OPM-MEG measurement systems are currently unavailable. After buying OPM sensors, we ourselves need to construct an MEG measurement system, such as a coil system for nulling the environmental magnetic field (Holmes et al., 2018; 2019; Iivanainen et al., 2019) and a cap or helmet to hold the sensors (Hill et al., 2020). If we only have a few OPM sensors (a common case for many OPM users), we must design the sensor array carefully depending on our purposes and the regions of interests (ROIs). For example, if we want to extract the brain activity at the motor cortex with five OPM sensors for a brain-computer interface (BCI), the sensors should be placed around the motor cortex. However, the accuracy of this expectation is unclear. Even if it is true, we do not know at which positions the sensors should be put.

Recently, Beltrachini et al. (2021) proposed a method to design OPM sensor arrays for minimizing source localization error. It sequentially determines the sensor positions to minimize the Cramér-Rao bound of the source localization error. However, because their scheme was developed for dipole methods (Muravchik et al., 2000), which approximate brain activities by a small number of current dipoles (Aine et al., 2000; Hari, 1991; Mosher et al., 1992), it cannot be used for distributed source methods, such as Minimum Norm Estimates (MNE) (Hämäläinen et al., 1993; Hämäläinen and Ilmoniemi, 1994; Ilmoniemi and Sarvas, 2019) or a Linearly Constrained Minimum Variance (LCMV) beamformer (Ilmoniemi and Sarvas, 2019; Van Veen et al., 1997). Distributed source methods assume distributed currents in the brain and are widely used in the MEG literature.

In this study, we propose a method that designs OPM sensor arrays for accurately estimating distributed currents. From a set of possible sensor positions, our method selects some positions so that the estimated cortical currents have accurate time-series at the ROIs. To achieve this aim, we focus on the MNE's resolution matrix (Hauk et al., 2022; Grave de Peralta-Menendez and Gonzalez-Andino, 1998), which represents the relationship between the true and estimated currents. The larger the diagonal elements in the resolution matrix are, the more accurate the time-series of the estimated current becomes. Therefore, we derived a recurrence formula of the resolution matrix and based on it, sequentially selected sensor positions so that the resolution matrix has large diagonal elements at the ROIs. We call this method a Sensor array Optimization based on Resolution Matrix (SORM).

We conducted simple and realistic simulation tests to evaluate its characteristics and efficacy for real OPM-MEG data. SORM selected sensor positions so that their leadfield matrices had high effective ranks as well as high sensitivities to ROIs. The sensor arrays designed by SORM were effective not only when we estimated the cortical currents by MNE but also when we did so by other methods: an LCMV beamformer (Van Veen et al., 1997) and the hierarchical Variational Bayesian method (hVB) (Sato et al., 2004; Yoshioka et al., 2008). Furthermore, we applied SORM to real OPM-MEG data to confirm its validity for real data. Based on these analyses, we believe that SORM is especially useful for accurately estimating ROIs' activities with a limited number of OPM sensors, such as BCI and the diagnosis of brain diseases.

2. Designing sensor arrays based on resolution matrix

In this section, we propose our SORM algorithm.

2.1. Assumption and purpose

We assume that we know the ROIs and that the possible OPM sensor locations have already been determined. Hereafter, for brevity, the set of possible OPM sensor locations is called the candidates. Given these ROIs and candidates, SORM selects the sensor positions so that the estimated cortical currents at the ROIs have accurate time-series.

2.2. Basic strategy

For this purpose, we focus on the resolution matrix (Hauk et al., 2022; Grave de Peralta-Menendez and Gonzalez-Andino, 1998) of MNE (Hämäläinen et al., 1993; Hämäläinen and Ilmoniemi, 1994). We explain this by starting from the basics of cortical current estimation.

In distributed source methods, MEG data are expressed as

$$B = GJ + E,\qquad(1)$$

where B is the $M \times T$ MEG data matrix, M is the number of channels, T is the number of time points, G is the $M \times N$ leadfield matrix, N is the number of current dipoles (vertices), J is the $N \times T$ cortical current matrix, and E is the $M \times T$ noise matrix.

Cortical current J is estimated by

$$\hat{J} = LB,\qquad(2)$$
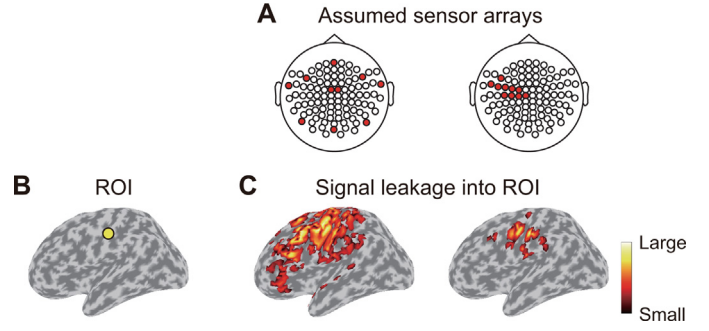
Fig. 1. Relationship between sensor array and signal leakage. (**A**) Assumed sensor arrays. Red circles indicate sensor positions. (**B**) ROI (a vertex in left somatosensory cortex). (**C**) Signal leakage into ROI from other areas. For each sensor array in **A**, we calculated MNE's resolution matrix and showed its absolute row vector values at ROI. Values over 0.3 of their maximum value are shown.

where L is an $N \times M$ matrix, called an inverse filter. In the case of MNE, L is calculated by

$$L = [G^{T}G + \lambda I]^{-1}G^{T},\qquad(3)$$

where λ is a regularization constant and I is the $N \times N$ identity matrix. By substituting Eq. (1) for B in Eq. (2), we obtain

$$\hat{J} = LGJ + LE.\qquad(4)$$

By putting

$$R = LG\qquad(5)$$

and taking the expectation of E, Eq. (4) is rewritten as

$$E[\hat{J}] = RJ.$$

R is an $N \times N$ matrix, called a resolution matrix (Hauk et al., 2022; Grave de Peralta-Menendez and Gonzalez-Andino, 1998), which represents the relationship between the true and estimated currents.

If R is an identity matrix, the current is perfectly estimated. However, R is strongly degenerate because its rank is $M << N$, and therefore it cannot be an identity matrix with rank N. The non-diagonal elements of R represent the signal leakage that occurs when estimating the current (Brookes et al., 2012; Colclough et al., 2015; Palva et al., 2018; Sato et al., 2018). Specifically, $R(a, b)$, where $b \neq a$, represents the signal leakage from vertex b to a. Therefore, to accurately estimate the current at vertex a, $R(a, a)$ needs to be larger than $R(a, b)$.

In the case of MNE, the resolution matrix is calculated from Eqs. (3) and (5) by

$$R = [G^{T}G + \lambda I]^{-1}G^{T}G.\qquad(6)$$

This is a symmetric matrix; that is, the signal leakage from vertex b to a and from a to b is identical. Because this equation does not include MEG data, we do not need to conduct MEG experiments to calculate the resolution matrices of MNE.

Figure 1 shows sample resolution matrices. We assumed two sensor arrays (Fig. 1A, red circles). For each, we calculated the resolution matrix of MNE by Eq. (6) (see Section 3 for detailed descriptions). We set ROI to a vertex in the left somatosensory cortex (Fig. 1B). To examine the signal leakage into the ROI from other areas, we show the absolute values of the row vector at the ROI in the resolution matrix (Fig. 1C): a so-called cross-talk function (Hauk et al., 2022). The signal leakage largely changed depending on the sensor arrays.

These considerations and results lead to SORM's basic strategy: determine the sensor positions so that the resolution matrix of MNE has larger diagonal elements than the non-diagonal elements at the ROIs.

2.3. Procedure to select sensor positions

To identify the relationship between the sensor positions and MNE's resolution matrix, we derived how the resolution matrix changes by adding a new sensor. Here we assume that each sensor measures a magnetic field along a single axis; each sensor has a single channel.

Suppose that we already set some sensors whose leadfield and resolution matrices of MNE are G and R. By adding a new sensor, R is changed to

$$R_+ = R + \frac{\lambda C^{-1} h^T h C^{-1}}{1 + h C^{-1} h^T}, \tag{7}$$

where $C = G^T G + \lambda I$ and h is a new row of the leadfield matrix corresponding to the new sensor [see Appendix A for the derivation of Eq. (7)]. Hereafter, a row of a leadfield matrix is called a sensitivity vector because it represents a sensor's sensitivity to each vertex. By defining a gain vector

$$x = C^{-1} h^T = [G^T G + \lambda I]^{-1} h^T, \tag{8}$$

Eq. (7) is rewritten as

$$R_+ = R + \frac{\lambda x x^T}{1 + x^T C x}.$$

Because $\lambda/(1 + x^T C x)$ is scalar, we focus on $x x^T$, which is an $N \times N$ matrix. The power of its diagonal elements at ROIs can be calculated by $x(n)^T x(n)$, where $n = [n_1, \cdots, n_v]$ represents the elements corresponding to ROIs. If $x(n)^T x(n)$ is large, the diagonal elements at ROIs in R_+ increase.

Based on these results, we propose the following procedure that selects the sensor positions from their candidates (Algorithm 1):

Algorithm 1 Select K sensor positions.

1: Set λ to a fixed value
2: Initialize $G^T G$ by $G^T G = \text{zeros}(N, N)$
3: for $k = 1 : K$
4:     Calculate $x = [G^T G + \lambda I]^{-1} h^T$ for each remaining sensor position
5:     Select the sensor position that maximizes $x(n)^T x(n)$
6:     Update $G^T G$ by $G^T G = G^T G + h^T h$
7: end

By default, regularization constant λ was set to

$$\lambda_0 = \frac{\text{tr}(G_{\text{all}}^T G_{\text{all}})}{N} \times 0.1, \tag{9}$$

where G_{all} is the leadfield matrix of all the candidate sensor positions.

3. Material and methods

We examined SORM's performance with two simulation tests: simple and realistic. The simple simulation test characterizes SORM's behavior, and the realistic simulation test evaluates its efficacy for real OPM-MEG data. Furthermore, we applied SORM to real OPM-MEG data. These analyses were conducted using VBMEG (https://vbmeg.atr.jp/), which is a MATLAB toolbox to estimate cortical currents from MEG and/or electroencephalography (EEG) data (Takeda et al., 2019).

3.1. Simple simulation test

3.1.1. Simulated experiment

Our simulation posited that 16 healthy adults participated in an OPM-MEG experiment. In it, they performed two tasks: motor and auditory, each of which consisted of 100 trials. During the tasks, we recorded the magnetic fields normal to their scalp surfaces (Z-axis) with OPM sensors.

3.1.2. Simulating brain activities

For simulating brain activities, we downloaded the 16 subjects' T1 images from the multi-subject, multi-modal neuroimaging dataset (OpenNEURO ds000117-v1.0.1) created by Wakeman and Henson (2015). From these images, we made brain models, which define 10,003 vertices on their cortical surfaces.

For the motor task, we selected two vertices from the left and right primary motor cortices. These selected vertices are referred to as sources in the simulation tests. We assigned currents at the sources and spatially smoothed them using a Gaussian filter whose standard deviation (SD) was 6 mm. For the auditory task, we selected two vertices, which are also referred to as sources in the simulation tests, from the left and right primary auditory cortices, assigned currents at the sources, and spatially smoothed them using the Gaussian filter. To highlight the effect of the signal leakage, the time-series of the currents were generated to be orthogonal between the sources so that the signal leakage between them affected their estimation accuracy. The amplitudes of the simulated currents were determined based on that of a current estimated from actual SQUID-MEG data.

3.1.3. Regions of interest

We set the ROIs based on the cortical parcellations defined in the HCP MMP 1.0 (Glasser et al., 2016). For the motor task, we set them to the primary motor cortices that are labeled "L_4_ROI" and "R_4_ROI" in the HCP MMP 1.0. For the auditory task, we set the ROIs to the early auditory cortices that are labeled "L_A1_ROI", "L_MBelt_ROI", "R_A1_ROI", and "R_MBelt_ROI" in the HCP MMP 1.0.

3.1.4. Candidates of sensor positions

We set the candidates of the OPM sensor positions based on those of the 102 magnetometers of an Elekta Neuromag Vectorview 306 system (Helsinki). From the multi-subject, multi-modal neuroimaging dataset, we derived the sensor positions of the magnetometers relative to the brains, moved them 12 mm away from the scalp surfaces, and used them as the candidates of the OPM sensor positions.

3.1.5. Making leadfield matrices

For each subject, we made a leadfield matrix of all the candidate sensor positions. From the T1 image, we constructed a 1-shell (cerebrospinal fluid [CSF]) head conductivity model. Based on it, we made a leadfield matrix by solving the Maxwell equations with a boundary element method (BEM). In this study, we assumed one-dimensional current dipoles normal to the cortical surface.

3.1.6. Selecting sensor positions

We selected the sensor positions by three methods: uniform, leadfield norm, and SORM. For all the methods, to select K sensor positions, we ranked all the candidate sensor positions and selected the first K positions.

In the uniform method, we manually ranked the sensor positions so that the sensors were uniformly distributed over the brain. This rank was fixed regardless of the subjects and the tasks.

In the leadfield norm method, we ranked the sensor positions based on their sensitivities to the ROIs. From the leadfield matrix of all the candidate sensor positions, we extracted the leadfield vectors corresponding to the ROIs, calculated their norms for the individual sensor positions, and ranked them in descending order of the norms.

For the SORM, we ranked the sensor positions by the order of the selected positions.

3.1.7. Simulating the OPM-MEG data

We set the number of OPM sensors to $1, \cdots, 50$. For each number, we simulated OPM-MEG data by Eq. (1). Observation noise E was made using Gaussian white noise whose SD was 2×10^{-13} T.

Figure 2 shows the simulated brain activities and sample OPM-MEG data at all the candidate positions. The signal-to-noise ratios (SNRs) of
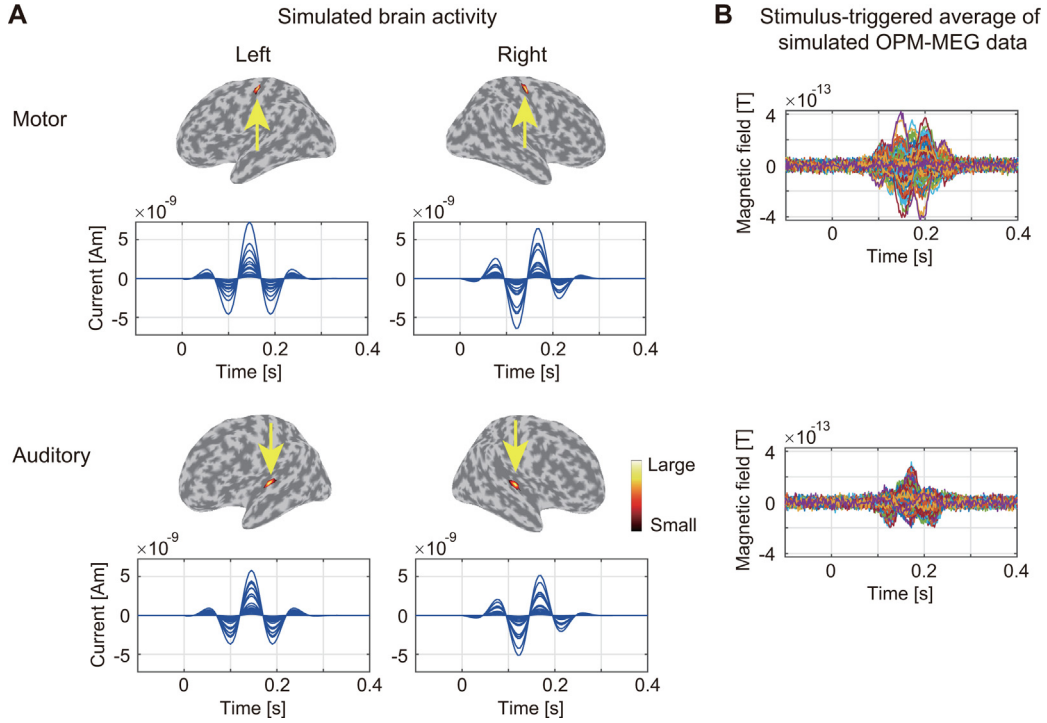
Fig. 2. Simulated brain activities and OPM-MEG data in simple simulation test. (**A**) Simulated brain activities. Top figures show amplitude distributions of simulated cortical currents averaged across time. Values over 0.3 of their maximum value are shown. Bottom figures show time-series of simulated cortical currents in left and right hemispheres. (**B**) Stimulus-triggered average of sample OPM-MEG data at 102 candidate positions.

the OPM-MEG data were -8.40 ± 1.57 dB and -14.08 ± 1.05 dB (mean $\pm$ SD) for the motor and auditory tasks. The SNRs were calculated by $10 \log_{10} P_s/P_n$, where P_s and P_n are the powers of $\boldsymbol{GJ}$ and $\boldsymbol{E}$ in Eq. (1), assuming that 102 OPM sensors were put at all the candidate positions.

3.1.8. Estimating the cortical currents

From the simulated OPM-MEG data, we estimated the cortical currents by three methods: MNE (Hämäläinen et al., 1993; Hämäläinen and Ilmoniemi, 1994), a LCMV beamformer (Van Veen et al., 1997), and hVB (Sato et al., 2004; Yoshioka et al., 2008).

MNE estimated the current by

$$\hat{\boldsymbol{J}} = [\boldsymbol{G}^{\mathrm{T}}\boldsymbol{G} + \lambda_{\mathrm{MNE}}\boldsymbol{I}]^{-1}\boldsymbol{G}^{\mathrm{T}}\boldsymbol{B},$$

where

$$\lambda_{\mathrm{MNE}} = \frac{\mathrm{tr}(\boldsymbol{G}^{\mathrm{T}}\boldsymbol{G})}{N} \times 0.1.$$

The LCMV beamformer estimated the current by

$$\hat{j}_n = \boldsymbol{l}_n\boldsymbol{B},$$

where $\hat{j}_n$ is the estimated current at vertex n and $\boldsymbol{l}_n$ is the $1 \times M$ inverse filter. The inverse filter was calculated by

$$\boldsymbol{l}_n = [\boldsymbol{g}_n^{\mathrm{T}}\tilde{\boldsymbol{D}}^{-1}\boldsymbol{g}_n]^{-1}\boldsymbol{g}_n^{\mathrm{T}}\tilde{\boldsymbol{D}}^{-1}, \tag{10}$$

where

$$\tilde{\boldsymbol{D}} = \boldsymbol{D} + \lambda_{\mathrm{BF}}\boldsymbol{I},$$

$$\lambda_{\mathrm{BF}} = \frac{\mathrm{tr}\,\boldsymbol{D}}{M} \times 0.1.$$

$\boldsymbol{g}_n$ is the $M \times 1$ leadfield vector for vertex n. $\boldsymbol{D}$ is the $M \times M$ covariance matrix computed between all the sensor pairs. We imposed regularization term $\lambda_{\mathrm{BF}}\boldsymbol{I}$, assuming that in real data analyses covariance matrix $\boldsymbol{D}$ often becomes rank deficient due to the noise reduction by independent component analysis (ICA) and a common average referencing for EEG.

In this study, LCMV beamformer indicates a scalar-type beamformer because we assumed a one-dimensional current dipole at each vertex.

hVB provides a framework to use the prior information on the current variance as soft constraints on the variance Sato et al. (2004); Yoshioka et al. (2008). It can use a variety of prior information, such as the uniform distribution, the fMRI activity, and a meta-analysis of fMRI studies (Suzuki and Yamashita, 2021). We used the uniform distribution as prior information on the current variance to set a confidence parameter, "bayes_parm.prior_weight," to 0.0001. This parameter controls the confidence in the prior information relative to the amount of data samples (ranging from 0 to 1) (Takeda et al., 2019).

The estimated currents were averaged across the trials.

3.1.9. Evaluating the accuracy of estimated source currents

For each condition (task, current estimation method, sensor array, and subject), we quantified the time-series accuracy of the estimated currents. At the sources, we calculated the correlation coefficients between the true and estimated currents and averaged them between hemispheres.

3.1.10. Statistical test

We compared the time-series accuracy of SORM with those of the uniform and leadfield norm methods. For each task, sensor array, and current estimation method, we performed a two-tailed Wilcoxon signed-rank test under the null hypothesis where the medians of the correlation coefficients were identical between SORM and the uniform/leadfield norm methods.

This is the multiple comparison problem, which we solved by controlling the false discovery rate (FDR). FDR manages the expected proportion of false positive findings among all the rejected null hypotheses (Benjamini and Hochberg, 1995). We estimated the q-values by Storey and Tibshirani's method (2003). From the distribution of the p-values, we first estimated the proportion of null p-values π_0, and based on π_0 we converted the p-values to q-values. The FDRs were controlled at 0.01.

3.1.11. Calculating contribution ratios in estimated source currents

To identify the factors responsible for the time-series accuracy, we examined the contribution ratios in the estimated source currents. We defined three kinds of contribution ratios: target, non-target, and noise. The target contribution ratio is that of the component originated from the left/right source in the estimated current at the left/right source; it represents the purity of the estimated currents. The non-target contribution ratio is that of the component originated from the right/left source in the estimated current at the left/right source; it represents the amount of signal leakage into a source from another source. The noise contribution ratio is that of the components originated from the noise [E in Eq. (1)].

To calculate the contribution ratios, we decomposed the simulated OPM-MEG data into components originated from the left source, the right source, and the noise. We separately converted these components into cortical currents using the inverse filters from Section 3.1.8. For the left source, the target contribution ratio was calculated by

$$cr_{\text{target}} = \frac{y_l}{y_l + y_r + y_n},$$

where y_l, y_r, and y_n are respectively the powers of the components originated from the left source, the right source, and the noise. The non-target contribution ratio was calculated by

$$cr_{\text{non-target}} = \frac{y_r}{y_l + y_r + y_n}.$$

The noise contribution ratio was calculated by

$$cr_{\text{noise}} = \frac{y_n}{y_l + y_r + y_n}.$$

In the same way, the contribution ratios were also calculated for the right source. Then, they were averaged between the left and right sources.

3.2. Analyzing real OPM-MEG, SQUID-MEG, and EEG data

For the realistic simulation test and applying SORM to real OPM-MEG data, we created and analyzed the OPM-MEG, SQUID-MEG, and EEG (OSE) dataset (https://vbmeg.atr.jp/nictitaku209/), which contains four subjects' OPM-MEG, SQUID-MEG, and EEG data during four tasks: auditory, motor, somatosensory, and resting-state. It also contains empty-room OPM-MEG data.

The four subjects participated in three recording sessions: OPM-MEG, SQUID-MEG and EEG, and MRI. The OPM-MEG data were recorded with 15 sensors (10 QZFM Gen-2 and five QZFM Gen-3, QuSpin Inc., U.S.), each of which recorded a magnetic field along two axes (Y and Z) (Supplementary material, SFig. 1). The SQUID-MEG and EEG data were simultaneously recorded with a whole-head 400-channel system (210-channel Axial and 190-channel Planar Gradiometers; PQ1400RM; Yokogawa Electric Co., Japan) and a whole-head 63-channel system (BrainAmp; Brain Products GmbH, Germany). Electrooculograms (EOGs) were also recorded simultaneously.

We preprocessed the OPM-MEG, SQUID-MEG, and EEG data for estimating the cortical currents. Because the OPM-MEG data contain large fluctuation below 8 Hz, we applied a lowpass filter at 40 Hz and a highpass filter at 8 Hz to all the data. Then we regressed out the EOG components from the data. For the EEG data, we took a common average reference and made the averages of the EEG data across the channels to 0.

From T1 images, we constructed 1-shell (CSF) and 3-shell (CSF, skull, and scalp) head conductivity models for the MEG and EEG data. Based on the models, we made leadfield matrices by solving the Maxwell equations with the BEM. Using the leadfield matrices, we estimated the cortical currents from the preprocessed OPM-MEG data. We also estimated the cortical currents from the SQUID-MEG and EEG (SQUID-MEG + EEG) data (Takeda et al., 2019).

3.3. Realistic simulation test

We conducted a realistic simulation test in the same way as the simple one except for procedures to simulate the brain activities and the OPM-MEG data. In this test, we simulated the former using the SQUID-MEG + EEG data during the auditory task and the latter using the SQUID-MEG + EEG data during the resting-state task and the empty-room OPM data. These procedures are described below.

3.3.1. Simulating brain activities

To simulate realistic brain activities, we used the cortical currents estimated from the SQUID-MEG + EEG data during the auditory task by hVB. We extracted currents at the left and right auditory cortices from a subject's cortical current. At the same sources as the simple simulation test, we assigned the currents and spatially smoothed them using a Gaussian filter whose SD was 6 mm. The amplitudes of the simulated currents were determined so that the reconstructed SQUID-MEG data from the simulated currents had the same amplitudes as the original one.

3.3.2. Simulating the OPM-MEG data

To simulate realistic OPM-MEG data, we used the cortical currents estimated from the SQUID-MEG + EEG data during the resting-state task and the empty-room OPM-MEG data. The OPM-MEG data was generated by

$$B = GJ + GJ_s + E$$

where J is the simulated brain activity produced in Section 3.3.1 and J_s is the spontaneous brain activity. J_s was extracted from the cortical currents estimated from the SQUID-MEG + EEG data during the resting-state task by MNE. E was generated from the empty-room OPM-MEG data. We generated surrogate data which had the same amplitude and a similar power spectrum with the preprocessed empty-room OPM-MEG data and used it as E.

Figure 3 shows the simulated brain activity and the sample OPM-MEG data at all the candidate positions. The SNRs of the OPM-MEG data were -18.52 ± 1.40 dB.

3.4. Applications to real OPM-MEG data

Finally, we evaluated the efficacy of SORM using real OPM-MEG data during the auditory task. The OPM-MEG data were recorded with 30 channels (15 sensors × 2 axes) (Supplementary material, SFig. 1). Here we regarded the 30 channels as the candidates of pseudo sensors. From them, we selected sensors by the uniform, the leadfield norm, and the SORM methods and estimated the cortical currents from the OPM-MEG data of the selected sensors. We quantified the time-series accuracy of the estimated currents by comparing them with the cortical currents estimated from the identical subjects' SQUID-MEG + EEG data during the auditory task. For each subject and vertex, we calculated the correlation coefficient of the cortical currents between the OPM and SQUID-MEG + EEG and averaged them within the ROIs (the early auditory cortices). We did not conduct statistical tests because of the small sample size (four subjects).

4. Results

4.1. Simple simulation test

To characterize the SORM behavior, we conducted a simple simulation test. We assumed that the 16 subjects performed two tasks: motor and auditory. During them, magnetic fields normal to their scalp surfaces were recorded with OPM sensors. We set the ROIs to the primary motor cortices for the motor task and the early auditory cortices for the auditory task (Fig. 4A).
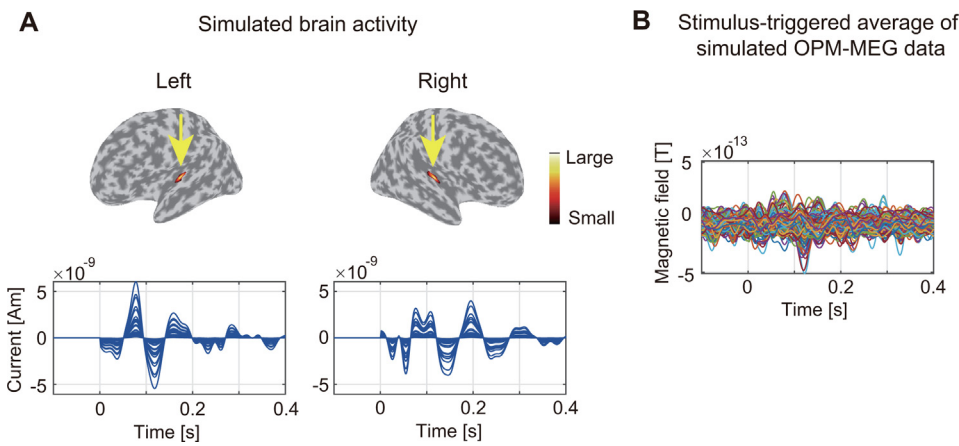
Fig. 3. Simulated brain activity and OPM-MEG data in realistic simulation test. (**A**) Simulated brain activity. Top figures show amplitude distributions of simulated cortical current averaged across time. Values over 0.3 of their maximum value are shown. Bottom figures show time-series of simulated cortical current in left and right hemispheres. (**B**) Stimulus-triggered average of sample OPM-MEG data at 102 candidate positions.
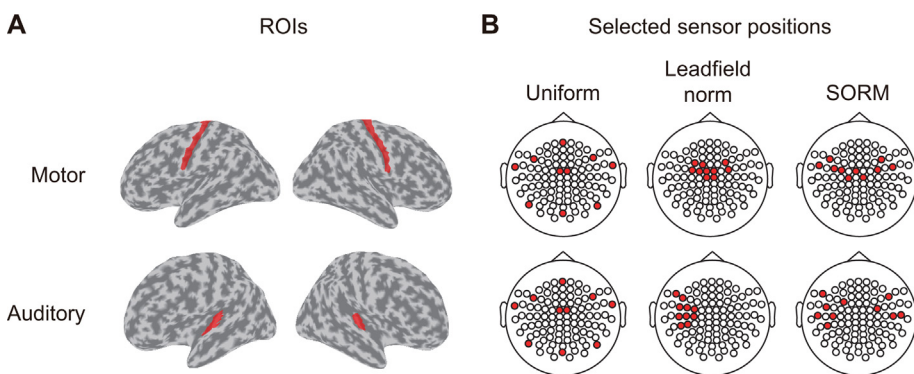
Fig. 4. Sensor arrays designed by uniform, leadfield norm, and SORM with 10 sensors. (**A**) ROIs. (**B**) Sensor arrays. Red circles indicate selected sensor positions. A subject's results are shown.

4.1.1. Designed sensor arrays

Figure 4B shows the sensor arrays designed by the uniform, leadfield norm, and SORM methods with 10 sensors. Compared with the uniform method, SORM prioritized the positions around the ROIs. On the other hand, compared with the leadfield norm method, SORM prioritized positions far from the ROIs.

To characterize the behaviors of these three methods, for each sensor array we examined the property of the leadfield matrix by two indices: sensitivity to the ROIs and the effective rank. To obtain sensitivity to the ROIs, we extracted from the leadfield matrix the submatrix corresponding to the ROIs and calculated its Frobenius norm. The effective rank represents the diversity of the sensitivity vectors across the selected sensor positions. We estimated it based on the singular values of the leadfield matrix (Roy and Vetterli, 2007).

Figure 5 shows the sensitivity to the ROIs and the effective rank for each sensor array. The uniform method showed high effective ranks but low sensitivities to the ROIs (Fig. 5, blue lines). In contrast, the leadfield norm method showed high sensitivities to the ROIs but low effective ranks (Fig. 5, red lines). SORM showed both high sensitivities and high effective ranks (Fig. 5, green lines). These results indicate that SORM selected sensor positions to increase both the sensitivity and the rank, while the other methods only increased one of them.

To comprehend the rationale of this result, we expressed $x^T x$ using the singular value decomposition (SVD) (Appendix B). It suggests that SORM tends to select a sensor position whose sensitivity vector has large values at ROIs and is in the null space of the existing sensors' leadfield matrix, heightening the effective rank of the new sensor array. This suggestion is consistent with Fig. 5. These results are intuitively interpreted as follows: a new sensor should be sensitive to the ROIs and represent outside of them to effectively suppress the signal leakage from the outside.
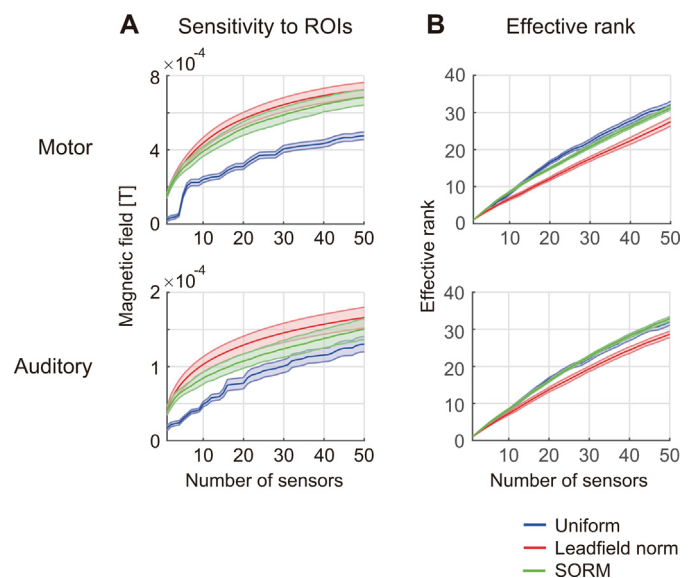
Fig. 5. Properties of leadfield matrices. (**A**) Sensitivity to ROIs. (**B**) Effective rank. Thick lines and shaded areas represent averages and SDs of values across subjects.

4.1.2. Accuracy of estimated source currents

For each sensor array, we simulated the OPM-MEG data and estimated the cortical current with MNE, the LCMV beamformer, and hVB. We evaluated the time-series accuracy of the estimated currents by the
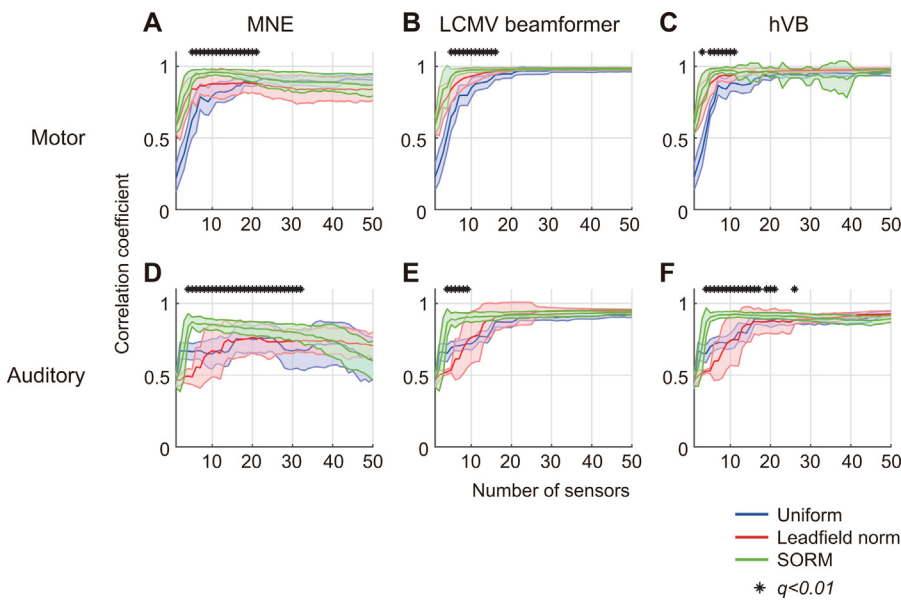
Fig. 6. Time-series accuracy of estimated source currents in simple simulation test. For each subject, we calculated correlation coefficients between true and estimated currents at left and right sources and averaged them between hemispheres. Thick lines and shaded areas represent averages and SDs of correlation coefficients across subjects. Asterisks indicate that correlation coefficients of SORM were significantly higher than those of uniform and leadfield norm methods ($q < 0.01$).

correlation coefficients between the true and estimated currents at the sources.

Figure 6 shows the time-series accuracy of the estimated currents. For all the current estimation methods, SORM outperformed the uniform and leadfield norm methods, especially when we used few sensors (< 15 sensors). This result indicates the efficacy of SORM for various current estimation methods.

On the other hand, when we used MNE and SORM, the time-series accuracy decreased as the number of sensors increased (Figs. 6A and D, green lines). This result indicates that using more sensors was not always better for MNE.

4.1.3. Contribution ratios in estimated source currents

To interpret the time-series accuracy, we calculated the contribution ratios in the estimated source currents during the auditory task. Figure 7 shows the contribution ratios averaged across the subjects. The target contribution ratios highly correlated with the time-series accuracy (their correlation coefficients were 0.94 ± 0.03) (Fig. 7, blue areas). This result suggests that the time-series accuracy mainly reflected the purity of the estimated currents.

When we used MNE, SORM drastically decreased the non-target contribution ratios as the number of sensors increased (Fig. 7G, red area). This result indicates that SORM effectively suppressed the signal leakage and increased the time-series accuracy, suggesting the validity of its algorithm.

On the other hand, when we used MNE and SORM, the time-series accuracy decreased as the number of sensors increased (Figs. 6A and D, green lines). The contribution ratios suggest that this was due to the increase of the noise contribution ratios (Fig. 7G, green areas). As the number of sensors increased, SORM added sensor positions where the data had low SNR. This increased the noise contribution ratios and decreased the time-series accuracy.

On the contrary, when we used the LCMV beamformer and hVB, the time-series accuracy did not greatly decrease (Figs. 6B, C, E, and F). The contribution ratios suggest that the LCMV beamformer suppressed the noise contribution ratios (Figs. 7B, E, and H, green areas), hVB suppressed the non-target and noise contribution ratios (Figs. 7C, F, and I, red and green areas), and as a result their time-series accuracy did not greatly decrease.

4.2. Realistic simulation test

To evaluate the efficacy of SORM for real OPM-MEG data, we conducted a realistic simulation test. In it, we used the real data to simulate the brain activities and noise. We used the same sensor arrays from the simple simulation test (Fig. 4B) because we set the ROIs to the same areas (the early auditory cortices) as the simple simulation test (Fig. 4A).

Figure 8 shows the time-series accuracy of the estimated currents. SORM outperformed the other methods, especially when we used the LCMV beamformer and just a few sensors (< 15 sensors). This tendency held unless the SNR was too low (Supplementary material, SFig. 2), indicating the efficacy of SORM for real OPM-MEG data.

4.3. Dependency on regularization constant

SORM has a hyperparameter: the regularization constant [λ in Eq. (8)], which was set to λ_0 [Eq. (9)] by default. We examined the dependency of SORM on the regularization constant by changing the regularization constant to $100\lambda_0$, λ_0, and $0.01\lambda_0$. For each constant, we designed the sensor array for the auditory task by SORM, simulated the OPM-MEG data during the auditory task, estimated the current by MNE, and evaluated the time-series accuracy.

Figure 9 shows the sensor arrays and the time-series accuracy for each regularization constant. They were almost the same across the constants, indicating that SORM did not largely depend on the regularization constant.

4.4. Application to real OPM-MEG data

Finally, we applied SORM to the real OPM-MEG data during the auditory task. We regarded the 30 OPM channels as the candidates of the pseudo sensors and from them selected some sensors (Fig. 10A). From the OPM-MEG data of the selected sensors, we estimated the cortical currents (Fig. 10B). The estimated currents at the ROIs (the early auditory cortices) were compared with those estimated from the same subjects' SQUID-MEG + EEG data during the auditory task (Fig. 10C).

Figure 10D shows the similarity of the estimated currents. Even when we used just a few pseudo sensors (< 10 sensors), SORM showed high similarity comparable with the leadfield norm method. That is, even with few pseudo OPM sensors, the leadfield norm method and SORM
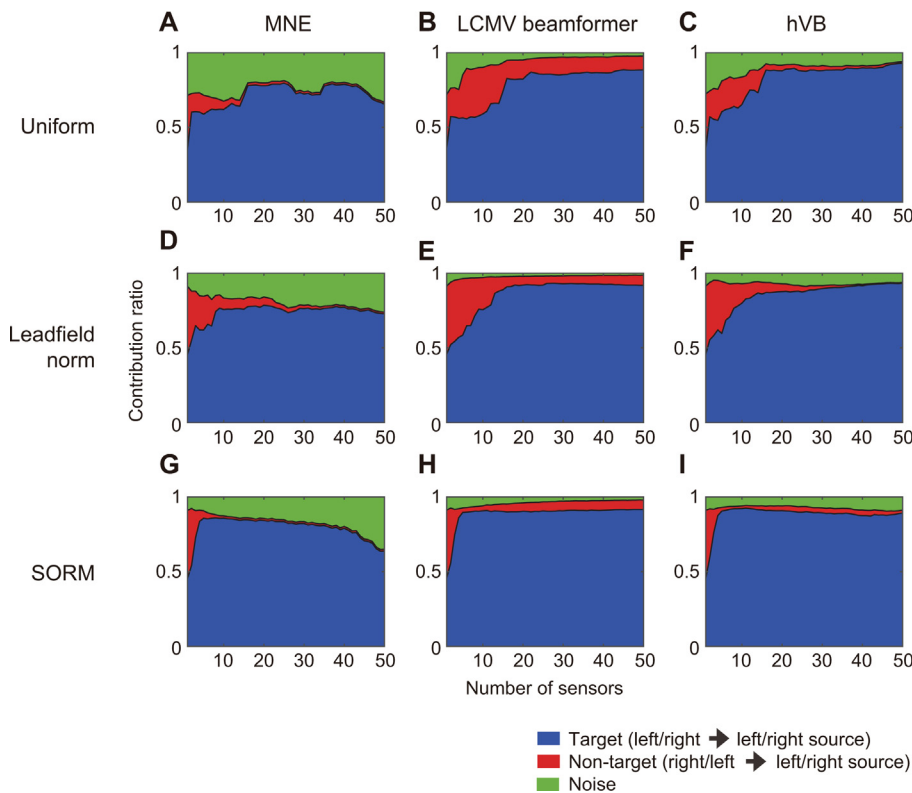
Fig. 7. Contribution ratios in estimated source currents of auditory task in simple simulation test. They were averaged across subjects.
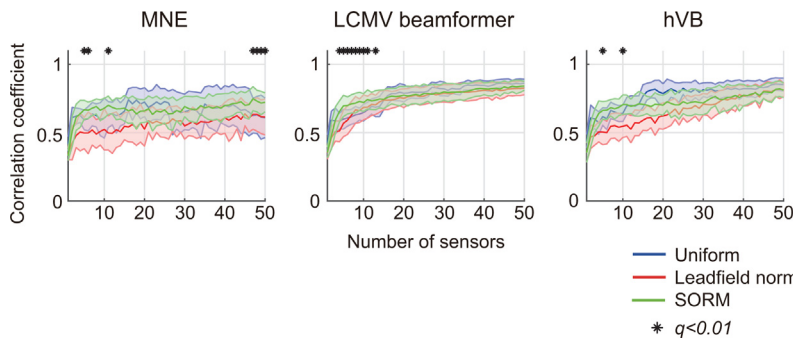
Fig. 8. Time-series accuracy of estimated source currents in realistic simulation test. For each subject, we calculated correlation coefficients between true and estimated currents at left and right sources and averaged them between hemispheres. Thick lines and shaded areas represent averages and SDs of correlation coefficients across subjects. Asterisks indicate that correlation coefficients of SORM were significantly higher than those of uniform and leadfield norm methods ($q < 0.01$).

enabled us to obtain the ROIs' currents resembling those estimated from a massive amount of data (400-ch SQUID-MEG and 63-ch EEG data). This result also indicates the efficacy of SORM for real OPM-MEG data.

5. Discussion

In this study, we proposed a SORM algorithm to design an OPM sensor array for accurately estimating the activity of ROIs. It sequentially selects sensor positions so that the resolution matrix of MNE has large diagonal elements at the ROIs. This strategy made the leadfield matrix have a high effective rank as well as high sensitivity to the ROIs (Fig. 5, green lines). Indeed, our mathematical consideration provided the rationale behind this result (Appendix B). Simulation tests showed that the SORM yielded higher time-series accuracy than the other methods, especially when we used a few sensors (< 15 sensors) (Figs. 6 and 8). Although SORM is based on MNE, the sensor arrays designed by SORM worked well regardless of the current estimation methods (Fig. 6). We also applied SORM to real OPM-MEG data and confirmed its efficacy for real data. These results suggest the efficacy of SORM when we want to accurately estimate ROIs' activity with a limited number of OPM sensors.

5.1. Methodological considerations

SORM sequentially selects the sensor positions from their candidates so that the MNE's resolution matrix has large diagonal elements at the ROIs. This is a combinatorial optimization problem, which we solved by a greedy algorithm. For example, when we select the 10 optimal sensor positions from the 102 candidates, we need to find one solution from $_{102}C_{10} > 2 \times 10^{13}$ combinations. Note that SORM does not find the optimal solution; it provides a sub-optimal one. By using the recurrence formula of the resolution matrix [Eq. (7)], SORM approximately solves this problem quickly. Indeed, it selected the 10 sensor positions from the 102 candidates within one minute using our computer [Intel(R) Xeon(R) CPU E5-2680 v2 @ 2.80GHz, 20 cores] and the selected positions outperformed those of the uniform and leadfield norm methods (Figs. 6 and 8). Since the SORM algorithm is very easy to implement, SORM is practical for a wide range of OPM users.

To accurately estimate ROIs' activities, SORM focuses on the diagonal elements at them in the MNE's resolution matrix and tries to increase them. However, this strategy also increased the non-diagonal elements and the diagonal elements (Supplementary material, SFig. 3), indicating that SORM enlarged the signal leakage into the ROIs as well as the
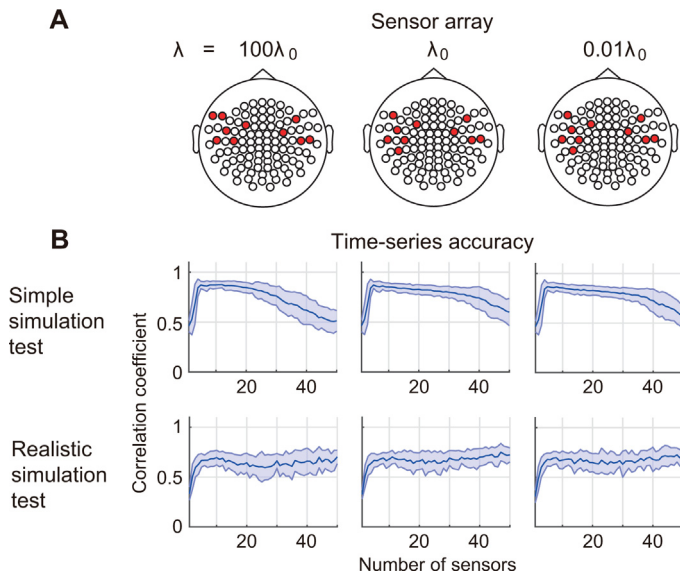
Fig. 9. Dependency of SORM on regularization constant. For each regularization constant, sensor array designed with 10 sensors (**A**) and time-series accuracy of source currents estimated by MNE (**B**) are shown for auditory task. Thick lines and shaded areas represent averages and SDs of correlation coefficients across subjects.

ROIs' activities. Nevertheless, SORM worked well in our simulation tests and applications to the OPM-MEG data (Figs. 6–10). As the number of sensors increased, the diagonal elements increased faster than the non-diagonal elements at the ROIs (Supplementary material, SFig. 3). As a result, the time-series of the estimated currents at the ROIs became more accurate as the number of sensors rose.

5.2. Spatial accuracy of estimated cortical currents

We focused on the temporal accuracy of the estimated cortical currents at ROIs and ignored their spatial accuracy. This is because SORM assumes that we have ROIs, meaning that we already know the information of the source locations. In this case, since evaluating the spatial accuracy is not very meaningful, we focused on the temporal accuracy and optimized the SORM algorithm to increase it.

On the other hand, the spatial accuracy of estimated currents has been widely evaluated in source imaging studies by localization accuracy and spatial extent (e.g. Hauk et al., 2022; Sekihara et al., 2005. Following these studies, we also evaluated the spatial accuracy of the estimated currents. SORM showed comparable spatial accuracy with the uniform and leadfield norm methods (Supplementary material, SFig. 4).

5.3. Contribution ratios

To identify the factors responsible for the time-series accuracy of the estimated source currents, we examined the contribution ratios in the
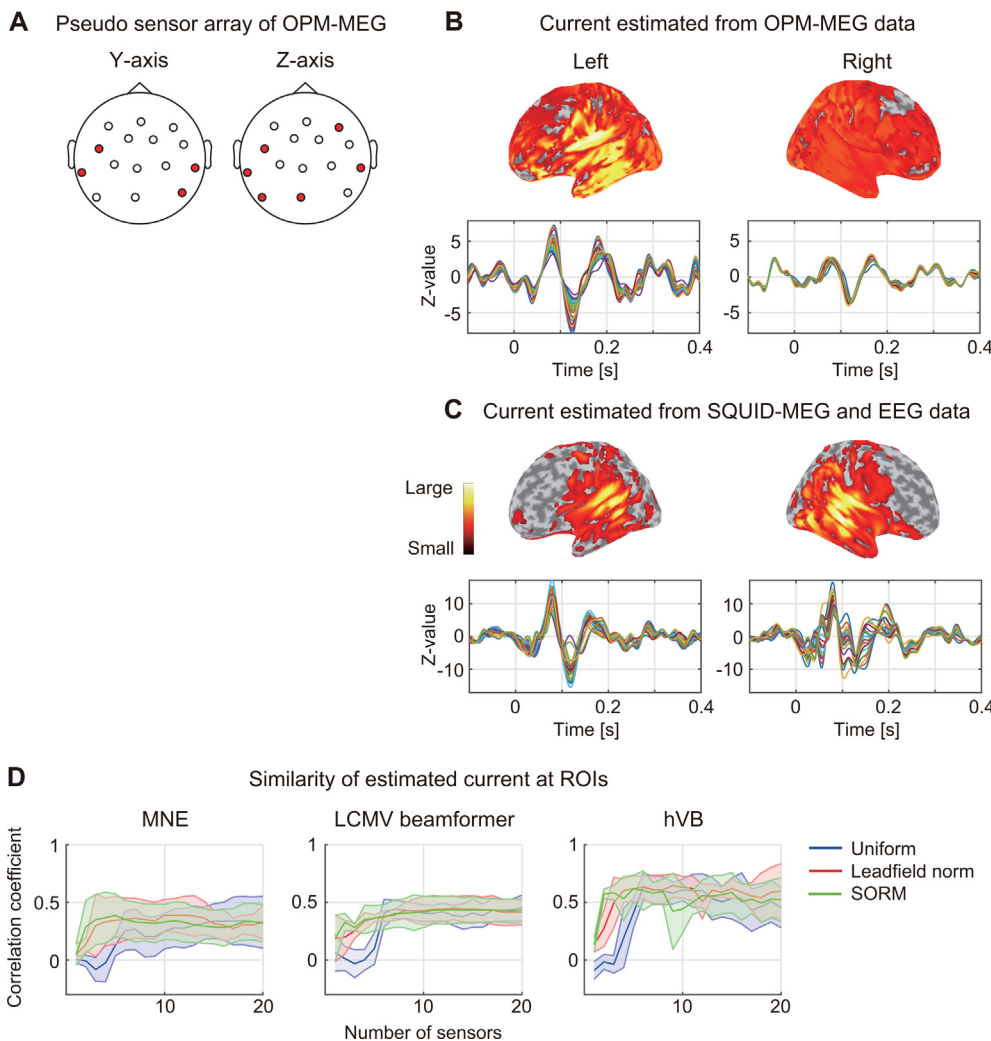
Fig. 10. Application to real OPM-MEG data. (**A**) Sensor array of 10 pseudo sensors designed by SORM. (**B**) Cortical current estimated from OPM-MEG data at selected pseudo sensors (**A**). (**C**) Cortical current estimated from SQUID-MEG + EEG data. In **B** and **C**, cortical currents during auditory task estimated by hVB are shown. Top figures show their amplitude distributions averaged across time. Values over 0.3 of their maximum value are shown. Bottom figures show time-series of currents at ROIs (early auditory cortices). In **A–C**, results of a subject are shown. (**D**) Similarity of currents at ROIs between OPM and SQUID-MEG + EEG data. For each subject and vertex, we calculated correlation coefficient of currents between OPM and SQUID-MEG + EEG data and averaged them within ROIs. Thick lines and shaded areas represent averages and SDs of correlation coefficients across subjects.

currents (Fig. 7). The contribution ratios suggest that the time-series accuracy (Fig. 6) mainly reflected the purity of the estimated currents (Fig. 7, blue areas). They also indicate that SORM effectively suppressed the signal leakage in the currents estimated by MNE (Fig. 7G, red area) and increased their time-series accuracy (Fig. 6D, green line), suggesting the validity of the SORM algorithm.

On the other hand, the contribution ratios revealed differences across the current estimation methods. For example, although the LCMV beamformer and hVB showed comparable time-series accuracy (Figs. 6E and F, green lines), the contribution ratios identified different strategies. The LCMV beamformer achieved high accuracy by suppressing the noise contribution ratio (Fig. 7H, green area), and hVB achieved it by suppressing the signal leakage (Fig. 7I, red area). In this way, the contribution ratios highlighted the differences across the current estimation methods and helped us select the best method for our purpose.

5.4. Extended usages

SORM uses MNE's resolution matrix because it can be calculated without MEG data [Eq. (6)]; that is, we do not need to conduct an MEG experiment in advance to design the sensor arrays. On the other hand, we can calculate the resolution matrices for other current estimation methods, such as the LCMV beamformer. Such adaptive filter methods need MEG data to calculate their resolution matrices. For example, the LCMV beamformer needs a covariance matrix computed between all the sensor pairs, and we need to estimate it by conducting a preparatory experiment or from existing data, such as open data. Once the covariance matrix is obtained, we can apply the same greedy algorithm as SORM (Section 2.3) except for steps 4 and 5. At these steps, instead of calculating $x(n)^{\mathrm{T}}x(n)$, we must calculate Eqs. (10) and (5) for each remaining sensor position to find the position that maximizes the diagonal elements at the ROIs in the resolution matrix.

SORM assumes that each OPM sensor measures a magnetic field along a single axis. However, current commercial OPM sensors can simultaneously measure a magnetic field along two or three axes. Indeed, the OPM-MEG data of the OSE dataset were recorded with the dual-axial sensors. With tri-axial OPM sensors, we can estimate 3D magnetic field vectors at the sensors. Furthermore, using tri-axial OPM sensors has theoretical advantages for current estimation (Brookes et al., 2021). SORM can be easily extended for tri-axial OPM sensors. In this case, each sensor has three channels. Using SORM, we can rank all the channels and the sensor positions based on the best channel in each sensor position and select the top K sensor positions.

5.5. Applicability

Since SORM designs the sensor arrays for accurately estimating ROIs' activity, it is suitable when we know the ROIs, such as BCI and diagnosing brain diseases. Recent proof-of-concept studies suggested the usefulness of OPM for non-invasive BCI (Wittevrongel et al., 2021) and diagnosing epilepsy (Vivekananda et al., 2020). For such purposes, simple MEG measurement systems with a few OPM sensors are practically helpful. For BCI, by setting the ROIs to the motor cortices, SORM can design a sensor array to accurately estimate a subject's motor intension. For the diagnosis of brain diseases, by setting ROIs to such affected regions as epileptic foci, SORM could design a sensor array to accurately monitor their activities.

Since SORM only relies on leadfield matrices [Eq. (8)], it can be applied to various problems where leadfield matrices (or forward models) exist, such as designing sensor arrays of EEG and near-infrared spectroscopy (NIRS). SORM can be used not only for the brain but also for the heart, muscles, and peripheral nerves, etc. For example, it could design an effective OPM sensor array for reconstructing cardiac activity from a magnetocardiography.

Data and code availability

The data used in this study are publicly available from the multi-subject, multi-modal neuroimaging dataset (OpenNEURO ds000117-v1.0.1, https://openneuro.org/datasets/ds000117/versions/1.0.1/) and the OSE dataset (https://vbmeg.atr.jp/nictitaku209/). The codes for performing SORM are available at https://github.com/RIKEN-AIP-CBDteam/Takeda2023_SORM.

Declaration of Competing Interest

The authors declare no competing interests.

Credit authorship contribution statement

Yusuke Takeda: Data curation, Formal analysis, Funding acquisition, Investigation, Methodology, Software, Validation, Visualization, Writing – original draft, Writing – review & editing. **Tomohiro Gomi:** Formal analysis, Investigation, Methodology, Validation, Writing – review & editing. **Ryu Umebayashi:** Formal analysis, Investigation, Methodology, Validation, Writing – review & editing. **Sadamu Tomita:** Formal analysis, Investigation, Methodology, Supervision, Validation, Writing – review & editing. **Keita Suzuki:** Data curation, Formal analysis, Investigation, Resources, Software, Writing – review & editing. **Nobuo Hiroe:** Data curation, Investigation, Resources, Writing – review & editing. **Jiro Saikawa:** Project administration, Supervision, Validation, Writing – review & editing. **Tatsuya Munaka:** Project administration, Supervision, Validation, Writing – review & editing. **Okito Yamashita:** Conceptualization, Formal analysis, Funding acquisition, Project administration, Resources, Supervision, Writing – review & editing.

Appendix A

In this section, we derive Eq. (7), which represents how the resolution matrix of MNE changes by adding a new sensor. Here we assume that each sensor has a single channel.

We use the following notations and equations:

1. M: number of existing channels (sensors)
2. N: number of vertices
3. G: $M \times N$ leadfield matrix of existing sensors
4. h: $1 \times N$ sensitivity vector of a new sensor
5. G_+: concatenated matrix of G and h ($G_+ = [G; h]$ in MATLAB notation)
6. $G_+^{\mathrm{T}} G_+ = G^{\mathrm{T}} G + h^{\mathrm{T}} h$
7. $C = G^{\mathrm{T}} G + \lambda I$
8. $[C + h^{\mathrm{T}} h]^{-1} = C^{-1} - \frac{C^{-1} h^{\mathrm{T}} h C^{-1}}{1 + h C^{-1} h^{\mathrm{T}}}$ [Derived from Eq. (11) in Faul and Tipping (2001)]
9. $R = C^{-1} G^{\mathrm{T}} G$: resolution matrix of existing sensors

Using the above notations and equations, the resolution matrix after adding a new sensor can be written:

$$\begin{aligned}
R_+ &= \left[G_+^{\mathrm{T}} G_+ + \lambda I \right]^{-1} G_+^{\mathrm{T}} G_+ \\
&= \left[G^{\mathrm{T}} G + \lambda I + h^{\mathrm{T}} h \right]^{-1} \left(G^{\mathrm{T}} G + h^{\mathrm{T}} h \right) \quad \text{(Using the 6-th equation)} \\
&= \left[C + h^{\mathrm{T}} h \right]^{-1} \left(G^{\mathrm{T}} G + h^{\mathrm{T}} h \right) \quad \text{(Using the 7-th equation)}
\end{aligned}$$

$$= \left(C^{-1} - \frac{C^{-1}h^{\mathrm{T}}hC^{-1}}{1 + hC^{-1}h^{\mathrm{T}}} \right) \left(G^{\mathrm{T}}G + h^{\mathrm{T}}h \right) \quad \text{(Using the 8-th equation)}$$

$$= C^{-1}G^{\mathrm{T}}G + C^{-1}h^{\mathrm{T}}h - \frac{C^{-1}h^{\mathrm{T}}hC^{-1}G^{\mathrm{T}}G}{1 + hC^{-1}h^{\mathrm{T}}} - \frac{C^{-1}h^{\mathrm{T}}hC^{-1}h^{\mathrm{T}}h}{1 + hC^{-1}h^{\mathrm{T}}}$$

$$= R + C^{-1}h^{\mathrm{T}}h - \frac{C^{-1}h^{\mathrm{T}}hC^{-1}(C - \lambda I)}{1 + hC^{-1}h^{\mathrm{T}}} - \frac{C^{-1}h^{\mathrm{T}}hC^{-1}h^{\mathrm{T}}h}{1 + hC^{-1}h^{\mathrm{T}}}$$

$$\text{(Using the 9-th equation)}$$

$$= R + C^{-1}h^{\mathrm{T}}h - \frac{C^{-1}h^{\mathrm{T}}h - \lambda C^{-1}h^{\mathrm{T}}hC^{-1} + hC^{-1}h^{\mathrm{T}}C^{-1}h^{\mathrm{T}}h}{1 + hC^{-1}h^{\mathrm{T}}}$$

$$= R + C^{-1}h^{\mathrm{T}}h - \frac{(1 + hC^{-1}h^{\mathrm{T}})C^{-1}h^{\mathrm{T}}h - \lambda C^{-1}h^{\mathrm{T}}hC^{-1}}{1 + hC^{-1}h^{\mathrm{T}}}$$

$$= R + \frac{\lambda C^{-1}h^{\mathrm{T}}hC^{-1}}{1 + hC^{-1}h^{\mathrm{T}}}.$$

Appendix B

To understand which kind of sensor position maximizes $x^{\mathrm{T}}x$, we express it by the singular vectors of the leadfield matrix of the existing sensors. We use the same notations and equations as in Appendix A. For simplicity, we set the ROIs to the whole brain.

SVD decomposes the leadfield matrix of existing sensors G as

$$G = U\Sigma V^{\mathrm{T}},$$

where U is an $M \times M$ orthogonal matrix, Σ is an $M \times N$ rectangular diagonal matrix, and V is an $N \times N$ orthogonal matrix. By using $G = U\Sigma V^{\mathrm{T}}$, C and C^{-1} can be written as

$$C = G^{\mathrm{T}}G + \lambda I$$
$$= V(\Sigma^{\mathrm{T}}\Sigma + \lambda I)V^{\mathrm{T}}$$

and

$$C^{-1} = V(\Sigma^{\mathrm{T}}\Sigma + \lambda I)^{-1}V^{\mathrm{T}}.$$

Gain vector x can be written as

$$x = C^{-1}h^{\mathrm{T}}$$
$$= V(\Sigma^{\mathrm{T}}\Sigma + \lambda I)^{-1}V^{\mathrm{T}}h^{\mathrm{T}}.$$

Consequently, we obtain

$$x^{\mathrm{T}}x = hV(\Sigma^{\mathrm{T}}\Sigma + \lambda I)^{-2}V^{\mathrm{T}}h^{\mathrm{T}}$$
$$= \sum_{n=1}^{N} \left(\frac{hv_n}{\sigma_n^2 + \lambda} \right)^2,$$

where v_n is the n-th column vector in V, hv_n is the dot product of h and v_n, σ_n is the n-th diagonal element in Σ, and $\sigma_n = 0$ if $n > M$. v_n and σ_n represent the orthogonal basis and its scale in G. Because $\sigma_n = 0$ for $n > M$, $v_{M+1}, \cdots, v_N$ represent the null space of G.

The above equation suggests that $x^{\mathrm{T}}x$ increases in the following two cases:

- h is large; that is, a sensor position has high sensitivity to the ROIs.
- hv_n is large when $\sigma_n = 0$; that is, the sensitivity vector of a sensor position is in the null space of the leadfield matrix of the existing sensors.

Supplementary material

Supplementary material associated with this article can be found, in the online version, at 10.1016/j.neuroimage.2023.120257

References

Aine, C., Huang, M., Stephen, J., Christner, R., 2000. Multistart algorithms for MEG empirical data analysis reliably characterize locations and time courses of multiple sources. Neuroimage 12, 159–172. doi:10.1006/nimg.2000.0616.

Beltrachini, L., von Ellenrieder, N., Eichardt, R., Haueisen, J., 2021. Optimal design of on-scalp electromagnetic sensor arrays for brain source localisation. Hum. Brain Mapp. 42, 4869–4879. doi:10.1002/hbm.25586.

Benjamini, Y., Hochberg, Y., 1995. Controlling the false discovery rate: A practical and powerful approach to multiple testing. J. R. Stat. Soc. Series B Stat. Methodol. 57, 289–300.

Boto, E., Bowtell, R., Krüger, P., Fromhold, T.M., Morris, P.G., Meyer, S.S., Barnes, G.R., Brookes, M.J., 2016. On the potential of a new generation of magnetometers for MEG: a beamformer simulation study. PLoS One 11, e0157655. doi:10.1371/journal.pone.0157655.

Boto, E., Meyer, S.S., Shah, V., Alem, O., Knappe, S., Kruger, P., Fromhold, T.M., Lim, M., Glover, P.M., Morris, P.G., Bowtell, R., Barnes, G.R., Brookes, M.J., 2017. A new generation of magnetoencephalography: room temperature measurements using optically-pumped magnetometers. Neuroimage 149, 404–414. doi:10.1016/j.neuroimage.2017.01.034.

Brookes, M.J., Boto, E., Rea, M., Shah, V., Osborne, J., Holmes, N., Hill, R.M., Leggett, J., Rhodes, N., Bowtell, R., 2021. Theoretical advantages of a triaxial optically pumped magnetometer magnetoencephalography system. Neuroimage 236, 118025. doi:10.1016/j.neuroimage.2021.118025.

Brookes, M.J., Leggett, J., Rea, M., Hill, R.M., Holmes, N., Boto, E., Bowtell, R., 2022. Magnetoencephalography with optically pumped magnetometers (OPM-MEG): the next generation of functional neuroimaging. Trends Neurosci. 45, 621–634. doi:10.1016/j.tins.2022.05.008.

Brookes, M.J., Woolrich, M.W., Barnes, G.R., 2012. Measuring functional connectivity in MEG: a multivariate approach insensitive to linear source leakage. Neuroimage 63, 910–920. doi:10.1016/j.neuroimage.2012.03.048.

Colclough, G.L., Brookes, M.J., Smith, S.M., Woolrich, M.W., 2015. A symmetric multivariate leakage correction for MEG connectomes. Neuroimage 117, 439–448. doi:10.1016/j.neuroimage.2015.03.071.

Faul, A.C., Tipping, M.E., 2001. Analysis of sparse bayesian learning. Advances in Neural Information Processing Systems 14. https://proceedings.neurips.cc/paper/2001/file/02b1be0d48924c327124732726097157-Paper.pdf

Glasser, M.F., Coalson, T.S., Robinson, E.C., Hacker, C.D., Harwell, J., Yacoub, E., Ugurbil, K., Andersson, J., Beckmann, C.F., Jenkinson, M., Smith, S.M., Van Essen, D.C., 2016. A multi-modal parcellation of human cerebral cortex. Nature 536, 171–178. doi:10.1038/nature18933.

Hämäläinen, M., Hari, R., Ilmoniemi, R.J., Knuutila, J., Lounasmaa, O.V., 1993. Magnetoencephalography - theory, instrumentation, and applications to noninvasive studies of the working human brain. Rev. Modern Phys. 65, 413–497.

Hämäläinen, M., Ilmoniemi, R.J., 1994. Interpreting magnetic fields of the brain: minimum norm estimates. Med. Biol. Eng. Comput. 32, 35–42. doi:10.1007/bf02512476.

Hari, R., 1991. On brain's magnetic responses to sensory stimuli. J. Clin. Neurophysiol. 8, 157–169. doi:10.1097/00004691-199104000-00004.

Hauk, O., Stenroos, M., Treder, M.S., 2022. Towards an objective evaluation of EEG/MEG source estimation methods - the linear approach. Neuroimage 255, 119177. doi:10.1016/j.neuroimage.2022.119177.

Hill, R.M., Boto, E., Rea, M., Holmes, N., Leggett, J., Coles, L.A., Papastavrou, M., Everton, S.K., Hunt, B.A.E., Sims, D., Osborne, J., Shah, V., Bowtell, R., Brookes, M.J., 2020. Multi-channel whole-head OPM-MEG: helmet design and a comparison with a conventional system. Neuroimage 219, 116995. doi:10.1016/j.neuroimage.2020.116995.

Holmes, N., Leggett, J., Boto, E., Roberts, G., Hill, R.M., Tierney, T.M., Shah, V., Barnes, G.R., Brookes, M.J., Bowtell, R., 2018. A bi-planar coil system for nulling background magnetic fields in scalp mounted magnetoencephalography. Neuroimage 181, 760–774. doi:10.1016/j.neuroimage.2018.07.028.

Holmes, N., Tierney, T.M., Leggett, J., Boto, E., Mellor, S., Roberts, G., Hill, R.M., Shah, V., Barnes, G.R., Brookes, M.J., Bowtell, R., 2019. Balanced, bi-planar magnetic field and field gradient coils for field compensation in wearable magnetoencephalography. Sci. Rep. 9, 14196. doi:10.1038/s41598-019-50697-w.

Iivanainen, J., Stenroos, M., Parkkonen, L., 2017. Measuring MEG closer to the brain: performance of on-scalp sensor arrays. Neuroimage 147, 542–553. doi:10.1016/j.neuroimage.2016.12.048.

Iivanainen, J., Zetter, R., Grön, M., Hakkarainen, K., Parkkonen, L., 2019. On-scalp MEG system utilizing an actively shielded array of optically-pumped magnetometers. Neuroimage 194, 244–258. doi:10.1016/j.neuroimage.2019.03.022.

Ilmoniemi, R.J., Sarvas, J., 2019. Brain signals: physics and mathematics of MEG and EEG. The MIT Press.

Mosher, J.C., Lewis, P.S., Leahy, R.M., 1992. Multiple dipole modelling and localization from spatio-temporal MEG data. IEEE Trans. Biomed. Eng. 39, 541–557. doi:10.1109/10.141192.

Muravchik, C., Bria, O., Nehorai, A., 2000. EEG/MEG error bounds for a dynamic dipole source with a realistic head model. Methods Inf. Med. 39, 110–113.

Palva, J.M., Wang, S.H., Palva, S., Zhigalov, A., Monto, S., Brookes, M.J., Schoffelen, J.M., Jerbi, K., 2018. Ghost interactions in MEG/EEG source space: a note of caution on inter-areal coupling measures. Neuroimage 173, 632–643. doi:10.1016/j.neuroimage.2018.02.032.

Grave de Peralta-Menendez, R., Gonzalez-Andino, S.L., 1998. A critical analysis of linear inverse solutions to the neuroelectromagnetic inverse problem. IEEE Trans. Biomed. Eng. 45, 440–448. doi:10.1109/10.664200.

Roy, O., Vetterli, M., 2007. The effective rank: a measure of effective dimensionality. EURASIP. https://www.eurasip.org/Proceedings/Eusipco/Eusipco2007/Papers/a5p-h05.pdf

Sato, M., Yamashita, O., Sato, M., Miyawaki, Y., 2018. 10.1371/journal.pone.0198806, Information spreading by a combination of MEG source estimation and multivariate pattern classification. PLoS One 13, e0198806.

Sato, M., Yoshioka, T., Kajihara, S., Toyama, K., Goda, N., Doya, K., Kawato, M., 2004. Hierarchical bayesian estimation for MEG inverse problem. Neuroimage 23, 806–826. doi:10.1016/j.neuroimage.2004.06.037.

Sekihara, K., Sahani, M., Nagarajan, S.S., 2005. Localization bias and spatial resolution of adaptive and non-adaptive spatial filters for MEG source reconstruction. Neuroimage 25, 1056–1067. doi:10.1016/j.neuroimage.2004.11.051.

Seymour, R.A., Alexander, N., Mellor, S., O'Neill, G.C., Tierney, T.M., Barnes, G.R., Maguire, E.A., 2021. Using OPMs to measure neural activity in standing, mobile participants. Neuroimage 244, 118604. doi:10.1016/j.neuroimage.2021.118604.

Shah, V.K., Wakai, R.T., 2013. A compact, high performance atomic magnetometer for biomedical applications. Phys. Med. Biol. 58, 8153–8161. doi:10.1088/0031-9155/58/22/8153.

Storey, J.D., Tibshirani, R., 2003. Statistical significance for genomewide studies. Proc. Natl. Acad. Sci. U S A. 100, 9440–9445. doi:10.1073/pnas.1530509100.

Suzuki, K., Yamashita, O., 2021. MEG current source reconstruction using a meta-analysis fMRI prior. Neuroimage 236, 118034. doi:10.1016/j.neuroimage.2021.118034.

Takeda, Y., Suzuki, K., Kawato, M., Yamashita, O., 2019. MEG source imaging and group analysis using VBMEG. Front. Neurosci. 13, 241. doi:10.3389/fnins.2019.00241.

Tierney, T.M., Holmes, N., Mellor, S., López, J.D., Roberts, G., Hill, R.M., Boto, E., Leggett, J., Shah, V., Brookes, M.J., Bowtell, R., Barnes, G.R., 2019. Optically pumped magnetometers: from quantum origins to multi-channel magnetoencephalography. Neuroimage 199, 598–608. doi:10.1016/j.neuroimage.2019.05.063.

Van Veen, B.D., van Drongelen, W., Yuchtman, M., Suzuki, A., 1997. Localization of brain electrical activity via linearly constrained minimum variance spatial filtering. IEEE Trans. Biomed. Eng. 44, 867–880. doi:10.1109/10.623056.

Vivekananda, U., Mellor, S., Tierney, T.M., Holmes, N., Boto, E., Leggett, J., Roberts, G., Hill, R.M., Litvak, V., Brookes, M.J., Bowtell, R., Barnes, G.R., Walker, M.C., 2020. Optically pumped magnetoencephalography in epilepsy. Ann. Clin. Transl. Neurol. 7, 397–401. doi:10.1002/acn3.50995.

Wakeman, D.G., Henson, R.N., 2015. A multi-subject, multi-modal human neuroimaging dataset. Sci. Data 2, 150001. doi:10.1038/sdata.2015.1.

Wittevrongel, B., Holmes, N., Boto, E., Hill, R., Rea, M., Libert, A., Khachatryan, E., Van Hulle, M.M., Bowtell, R., Brookes, M.J., 2021. Practical real-time MEG-based neural interfacing with optically pumped magnetometers. BMC Biol. 19, 158. doi:10.1186/s12915-021-01073-6.

Yoshioka, T., Toyama, K., Kawato, M., Yamashita, O., Nishina, S., Yamagishi, N., Sato, M., 2008. Evaluation of hierarchical bayesian method through retinotopic brain activities reconstruction from fMRI and MEG signals. Neuroimage 42, 1397–1413. doi:10.1016/j.neuroimage.2008.06.013.